

Technical Paper

Effect of loading eccentricity on the ultimate lateral resistance of twin-piles in clay

Zihao Zhao^{a,b,c}, Hao Zhang^a, Lijun Ke^{b,c}, Guoqing Zhao^a, Suyun Meng^a,
Fengyuan Wu^{a,*}, Jim Shiau^d

^a School of Civil Engineering, Shenyang Jianzhu University, Shenyang 110168, China

^b Key Laboratory of Ministry of Education for Geomechanics and Embankment Engineering, Hohai University, Nanjing 210098, China

^c Jiangsu Research Center for Geotechnical Engineering Technology, Hohai University, Nanjing 210098, China

^d School of Civil Engineering and Surveying, University of Southern Queensland, Toowoomba, QLD, Australia

Received 23 August 2021; received in revised form 27 January 2022; accepted 25 February 2022

Available online 16 March 2022

Abstract

This paper studies the effect of loading eccentricity and pile spacing on the ultimate lateral soil resistance of twin-piles using finite element limit analysis and analytical upper bound plasticity methods. Two kinematic mechanisms corresponding to the failure modes produced by the advanced finite element simulations are postulated with different eccentricity and pile spacing cases. Comparisons have shown excellent agreements between the two approaches. A series of parametric studies are then subsequently performed. Numerical results have shown that loading eccentricity considerably affects ultimate lateral soil resistance, leading to a maximum reduction of 50%. In addition, the curve of normalised pile resistance versus pile spacing ratio is dissimilar to that without considering the effect of loading eccentricity. The proposed solutions and failure mechanisms in this study will provide a deepened insight on the performance of twin-pile group under eccentric loads.

© 2021 Production and hosting by Elsevier B.V. on behalf of The Japanese Geotechnical Society. This is an open access article under the CC BY-NC-ND license (<http://creativecommons.org/licenses/by-nc-nd/4.0/>).

Keywords: Piles; Twin-pile group; Lateral soil resistance; Clays; Numerical limit analyses; Analytical upper bound plasticity calculations; Loading eccentricity

1. Introduction

The design of pile foundation requires accurate evaluation of the ultimate lateral resistance on pile and pile groups subjected to external loads. Many researchers have investigated the response of individual piles to lateral loading or movement based on full-scale tests or physical modellings (see e.g., Matlock 1970; Reese and Welch 1975; Pan

et al. 2000; Zhao and Wang 2018; Ueda et al. 2019), analytical calculations (see e.g., Poulos 1971; Murff and Hamilton 1993; Zhang et al. 2013; Yu et al. 2015, 2017) and numerical analyses (see e.g., Brown and Shie 1991; Hazzar et al. 2017; Teramoto et al. 2018; Zhao et al. 2019).

It is commonly accepted that the ultimate soil resistance per unit length p_u on an isolated pile increases with depth till it reaches a maximum value at acritical depth, beyond which the soil resistance remains constant where the collapse is confined to a horizontally plastic flow type. For this, the ultimate soil resistance is uniformly mobilised along the pile length, and therefore only a two-dimensional plane-strain horizontal section of the pile shaft needs to be considered. To consider the more realistic flow-

Peer review under responsibility of The Japanese Geotechnical Society.

* Corresponding author.

E-mail addresses: ayzihaozhao@163.com (Z. Zhao), zh18843973567@163.com (H. Zhang), kelijun93@163.com (L. Ke), zhaoguoqing@cugb.edu.cn (G. Zhao), mengsuyun@cugb.edu.cn (S. Meng), fywucivil@163.com (F. Wu), jim.shiau@usq.edu.au (J. Shiau).

<https://doi.org/10.1016/j.sandf.2022.101126>

0038-0806/© 2021 Production and hosting by Elsevier B.V. on behalf of The Japanese Geotechnical Society.

This is an open access article under the CC BY-NC-ND license (<http://creativecommons.org/licenses/by-nc-nd/4.0/>).

around soil resistance, some researchers have provided analytical solutions within the framework of rigid-plastic limit analysis. Randolph and Houlsby (1984) presented two-dimensional lower and upper-bound plasticity solutions and derived the exact solution for rough piles. Later, other researchers (see e.g., Murff et al. 1989; Christensen and Niewald 1992; Martin and Randolph 2006; Klar and Osman 2008) proposed several improved solutions to Randolph and Houlsby's solution, by taking account for lower pile-soil adhesions (adhesion factor ranges from 0 to 1). So far, the combined upper-bound mechanism presented by Martin and Randolph (2006) was recognized as the best solution for a whole range of pile-soil adhesions.

While the ultimate soil resistance of individual piles in clay was well established, rather limited studies have been conducted with respect to the pile group that is commonly used in practice. To consider the group effects, a number of experimental investigations on pile groups were performed by several researchers, including full-scale lateral load tests (e.g. Matlock et al. 1980; Brown et al. 1987, 1988; Rollins et al. 2006), model tests (e.g. Cox et al. 1984; Chandrasekaran et al 2009; Su et al. 2016) and centrifuge model tests (e.g. McVay et al. 1994, 1996, 1998; Ilyas et al. 2004).

Owing to the complexity of fully instrumented lateral load tests as well as budget limitation, a comprehensive investigation with extensive parameters may be prohibitive. As a result, mathematical tools such as using advanced finite elements and limit analysis methods have become useful alternatives. In recent years, Georgiadis et al. (2013a) utilised such approaches to investigate the ultimate lateral soil resistance of the twin-pile group. They then established a relationship between the pile capacity and the pile spacing that accounts for the effect of loading direction (Georgiadis et al. 2013b). Later, other researches extended the solutions of ultimate soil resistance to the cases of a row of piles (Georgiadis et al. 2013c), tripod piles (Zhao et al. 2017a), tetrapod piles (Zhao et al. 2017b) and other square pile group configurations (Pham et al. 2019; Sheil, 2021). Georgiadis et al. (2020) and Zhao and Gao (2019) further investigated the effect of torsion on the undrained lateral soil resistance of individual pile and tripod piles, respectively.

It is noted that the effect of loading eccentricity was not studied in the above-mentioned works. When the horizontal load does not pass through the geometrical center of the pile group, the effect of loading eccentricity on the ultimate lateral soil resistance cannot simply be neglected. To fill this gap, the limiting lateral resistance of twin-pile group under a general eccentric load is determined in this paper by using two-dimensional plane-strain analytical and numerical limit analyses. Based on the failure contours identified via numerical simulations, two kinematic mechanisms were constructed as the basis for the subsequent analytical upper bound calculations. The analytical upper bound solutions were validated via numerical upper and lower-bound limit analysis methods, while the effect of

the pile spacing is investigated with the upper bound method only. In order to gain deeper insight on the governing failure mode due the effect of loading eccentricity and different pile group geometries, a series of numerical investigations for various pile spacing are presented in the paper.

2. Numerical limit analyses

Finite element limit analysis (FELA) is a powerful computational technique that combines the technique of finite element discretisation for handling complex geotechnical problems and the classical limit theorems of upper and lower bound analyses. Finite element upper- and lower-bound limit analyses provide quasi-rigorous bounds that bracket the exact solutions from below and above, and they shall always be introduced as a pair. The difference between lower and upper bounds can offer a measure of the discretisation error in the result and can be narrowed to a rather limited interval by using more elements.

The formulations used in FELA algorithms historically stem from the pioneering work of Lysmer (1970), Anderheggen and Knopfel (1972) and Sloan (1988, 1989) who used linear programming and discontinuous stress or velocity field to solve the stability problems. With the development of the method for numerical implementation and the optimisation algorithm, FELA algorithm has evolved significantly with incorporation of nonlinear optimisation technique in Lyamin and Sloan (2002a, 2002b) and Krabbenhoft et al. (2005, 2007). Their used efficient stress-based (lower bound) and velocity-based (upper bound) element formulations in the FELA framework with second-order cone programming and adaptive meshing technique, which are available in the software program OptumG2. Both formulations lead to convex mathematical programs, which can be integrated in the form as follows:

$$\begin{aligned} & \text{maximise } \lambda \\ & \text{subject to } A\sigma = p_0 + \lambda p \\ & f_i(\sigma) \leq 0, \quad i = \{1, \dots, N\} \end{aligned} \quad (1)$$

where λ is the load multiplier, σ is the vector of stress variables, A is the matrix of equality constraint coefficients, p_0 and p are the vectors of prescribed and optimisable forces respectively, f_i is the yield function for stress set i , and N is the number of stress nodes. The technique has been successfully applied to a number of geotechnical stability problems (Shiau and Smith 2006, Shiau et al. 2008, Shiau et al. 2016, Shiau and Al-Asadi 2020). More details of the computational formulations of FELA in OptumG2 can be found in Krabbenhoft et al. (2017).

2.1. Finite element model and material properties

A two-dimensional plane-strain numerical model used to study the effect of loading eccentricity on the lateral resistance of the twin-pile group in undrained

elastic-perfectly plastic soil medium is presented in Fig. 1. The problem comprises the soil domain and two infinitely long rough piles of diameter $D = 1$ m with center-to-center spacing s . An eccentric load F was applied at a distance of e from the center point of twin-pile group, in which two individual piles were connected by a rigid cap. The direction of the lateral load is perpendicular to the pile-to-pile axis.

Fig. 2 presents a model domain of the twin-pile problem for using OptumG2. It is expectedly led to quasi-rigorous bounds on the exact solution. Two-dimensional triangle elements with upper bound and lower bound element formulations were used to discretise both the soil domain and the pile sections. The upper and lower bound elements are constructed directly based on the upper and lower bound principles and it is expected that quasi-rigorous bounds on the exact solution can be achieved. Five adaptive iterations are adopted for mesh refinement with the number of element increasing from 100 to 20000. All boundaries were fixed along both the normal and shear directions, and positioned far enough from the center of the pile group to eliminate boundary effects. Several pilot analyses would suggest that the dimension of the two-dimensional model be $10D$ for the side boundaries and $20D$ for the top and bottom boundaries. The two piles are regarded as linear elastic material while the soil is considered as an elastoplastic Tresca material.

The material parameters in this study are to follow Georgiadis et al. (2013a): undrained shear strength of soil material $s_u = 100$ kPa, Young's modulus of soil material $E_u = 2 \times 10^4$ kPa, Poisson's ratio of soil material $\nu_u = 0.495$, Young's modulus of pile material $E_p = 2.9 \times 10^7$ kPa, and Poisson's ratio of pile material $\nu_p = 0.1$. As the analyses are theoretically based on the plastic bounding theorems with the assumption of small strains, the ultimate load would not be influenced by the initial stresses or deformations. Hence, the choice of the stiffness parameters does not affect the stability outcomes (Sloan 2013).

Owing to the fact that the capped twin-pile always translate laterally as a rigid body, the eccentric load applied on the pile cap can be distributed proportionally to the center

of the two piles in simulations (Fig. 2). The forces imposed on every piles can be calculated as functions of F , e and s :

$$F_l = F(0.5 - e/s) \quad (2)$$

$$F_r = F(0.5 + e/s) \quad (3)$$

where F_l is the force distributed to the left-hand side (LHS) of the piles and F_r is the force distributed to the right-hand side (RHS) of the piles. It is noted that Eqs. (2) and (3) were obtained by considering the force and moment equilibrium conditions. According to the computational algorithms implemented in OptumG2, the forces imposed (F_l and F_r) were set as multiplier loads, which are amplified until a state of incipient collapse is attained during the process of analysis. The factor by which the multiplier load is to be amplified till a collapse state is referred to as the collapse multiplier. The ultimate load is obtained by multiplying the initially prescribed load with the collapse multiplier. This is actually one of the appealing advantage of finite element limit analysis in dealing with geotechnical structure problems. It is possible to compute the limit load directly without having to perform a step-by-step elastoplastic analysis (Sloan 2013). In addition, the calculated limit loads were all presented in the normalised form (average pile resistance factor $N_p = F/2s_uD$), which eliminates the dependency of the outcomes on the soil strength parameter and the pile geometry.

2.2. The ultimate pile resistance factor N_p

Fig. 3 shows the ultimate pile resistance factor N_p against normalised eccentricity e/s (ratio of eccentricity to pile spacing). Therein, three representative pile spacing cases ($s/D = 1.2, 1.8$ and 2.5) are presented for the upper-bound finite-element limit analysis. Numerical results have shown that the average pile resistance generally decreases as the eccentricity increases, except that the eccentricity is extremely small, where a horizontal section of maximum capacity is presented. One possible reason for this phenomenon could be due to the unchanged shape of failure surfaces with such low eccentricities. Note that the response is similar to the twin-pile mode presented in Georgiadis et al. (2013a).

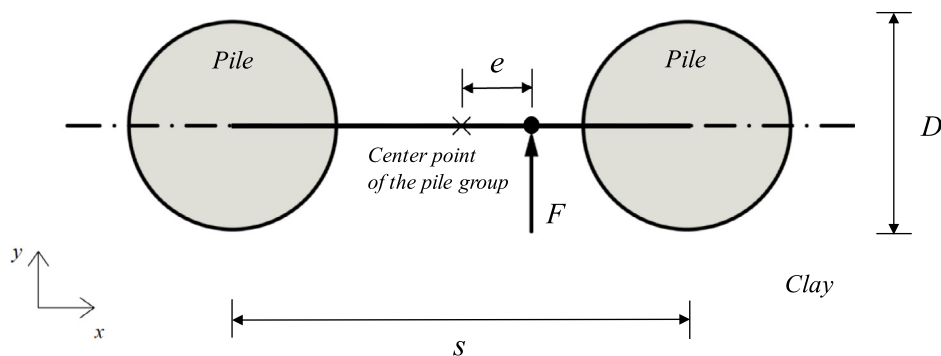


Fig. 1. Problem definition: Twin-pile subjected to an eccentric lateral load.

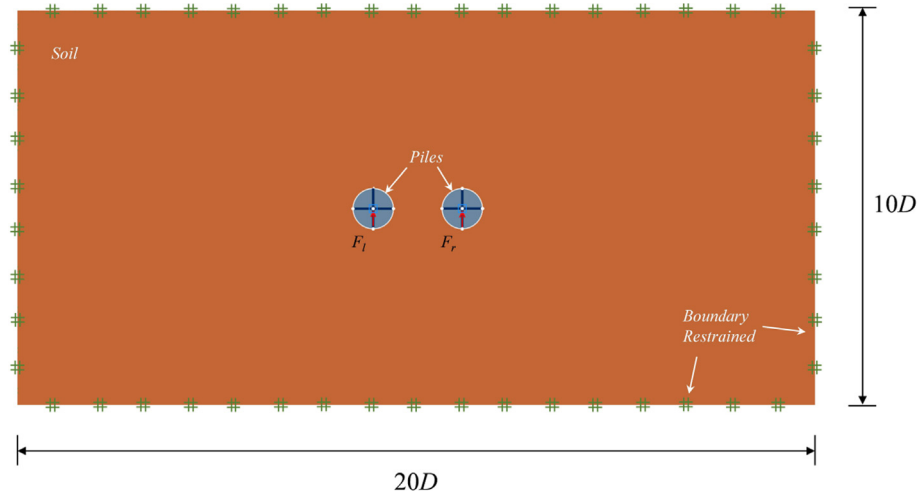


Fig. 2. Geometry of the two dimensional twin-pile model.

For the case of $s/D = 1.2$ (see Fig. 3(a)), numerical results have shown that the decrease of N_p can be divided into two stages (stages A and B) based on the slope of curve segments. Variation of the stages can be further identified by considering different failure modes associated with various e/s . As the power dissipation in soil mass provides a good indicator of the intensity of plastic deformation, the contour plot of internal power dissipation is always used to reveal the mode of collapse despite that the actual values of the contour are not important in such a perfectly plastic material model. Fig. 4 presents two typical finite-element meshes and power dissipation contours for the cases of $e/s = 0.25$ and 0.5 . This represents two distinct failure modes (modes A and B) corresponding to stages A and B, respectively. As the eccentricity is small, the two piles move in the same direction at a rate that is approximately equal, and the effect of the loading eccentricity can be negligible. When the eccentricity increase beyond $e = 0.02 s$ (stage A in Fig. 3(a)), the force imposed on the RHS pile is obviously larger than the force on the LHS pile, which renders most of the resistance with soils mobilised associated with the RHS pile. In addition to this, the soil movement involved in the twin-pile system is mostly controlled by the RHS pile. As a result, a lopsided failure mode (mode A) develops (see Fig. 4(a)), in which the LHS pile is excluded by the exterior slip surface. As the eccentricity ratio $e/s > 0.37$ (stage B in Fig. 3(a)), the failure mode changes to mode B, where two piles tend to move in the opposite direction under the influence of increasing eccentricity. This is demonstrated in Fig. 4(b).

As for the case of $s/D = 1.8$ (Fig. 3(b)), it is observed that the curve of N_p with e/s transforms to a single-segment descent type. As eccentricity increases, after a short horizontal section of maximum N_p , the decrease of N_p undergoes only one stage (stage A), which corresponds to the failure mode A. When the normalised pile spacing s/D increases to 2.5 (see Fig. 3(c)), pile-to-pile interaction effects become trivial, and the failure mode generally

degenerates to the well-known single-pile failure mode for most e/s (Randolph and Houlsby 1984, Martin and Randolph 2006).

Four representative failure modes (from the observation of power dissipation contours) are identified across wide ranges of e/s and s/D . Two of them were reported and well-defined in previous literatures (single-pile mode and twin-pile mode) and the other two are newly presented (mode A and mode B) in this paper. This new finding provides reasonable explanations for the variation in Fig. 3 and therefore lead to the establishment of kinematic mechanisms in the following analytical upper bound calculations.

3. Analytical upper bound solutions

The analytical approach, for predicting the bearing capacity of twin-pile groups, employed in this study is based on the upper bound theorem of limit analysis, which is a common-seen mathematical treatment of geotechnical stability problems (Georgiadis et al. 2013a, 2013b, 2013c; Yu et al. 2015, 2017). Similar to the traditional limit equilibrium method, the analytical upper bound requires a prior assumption of failure mechanism. The method assumes the soil to be perfectly plastic with an associated flow rule. For a “displaced” field, the upper bound solution is determined by equating the power expended by the external loads to the power dissipated internally by the plastic deformations. Therefore, it is significant to construct a correct kinematic mechanism that gives the accurate estimation of the upper bound solution.

Referring to the collapse modes observed previously in FELAs, four kinematic mechanisms will be presented in this section. First two mechanisms (the single-pile mechanism and the twin-pile mechanism) have been defined in the previous studies (Martin and Randolph 2006; Georgiadis et al. 2013a), while the other two mechanisms are newly proposed for eccentrically loaded cases: the first new kinematic mechanism gives the optimal upper bound

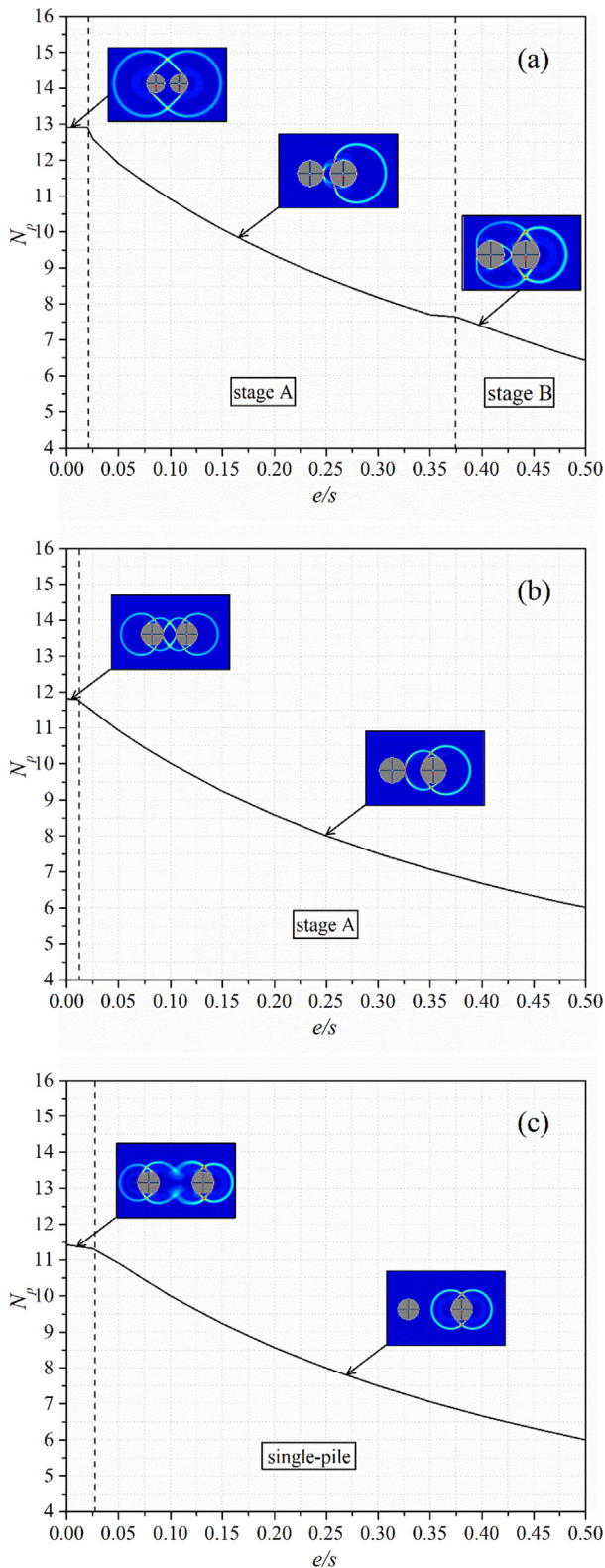


Fig. 3. Variations of the average pile resistance factor N_p with the normalised eccentricity e/s for (a) $s/D = 1.2$, (b) $s/D = 1.8$ and (c) $s/D = 2.5$. Results from FELA-UB.

solution for certain spacing cases with small eccentricities, while the second gives the optimum solution for greater eccentricities.

3.1. Existing mechanism for single piles

For large-spaced pile groups, the ultimate soil resistance is equivalent to a single-pile solution. The kinematic mechanism of such a single pile response has been well-presented by [Martin and Randolph \(2006\)](#). The deformation pattern has fourfold symmetry, so only one quarter of the mechanism is shown in [Fig. 5](#). Four separate regions can be identified according to the different shear flow patterns. Two of them behave as in rigidity: the region ABC moves rigidly with the pile while the region HXI entirely rotates around the point O. The other two regions (CAGFED and AHIFG) are plastically deforming parts in which the velocities are determined by the velocity jump along the discontinuities at the region boundaries. Two geometrical parameters λ and β are introduced to define the mechanism and obtain the minimum values for the lateral bearing capacities of single piles. The derivation of the energy dissipations can be found in [Martin and Randolph \(2006\)](#).

3.2. Existing mechanism for two side-by-side piles

[Georgiadis et al. \(2013a\)](#) constructed upper bound velocity fields based on the displacement finite element results for a group of two side-by-side piles that are horizontally loaded in clay. The proposed mechanism covers the cases with extremely small eccentricity, and it corresponds to the “twin-pile mode” that was identified in the FELA. This mechanism is shown in [Fig. 6](#), and is considered as an extension of the single-pile mechanism proposed by [Martin and Randolph \(2006\)](#). It is noted that the velocity flow pattern in the outer portion of the mechanism inherits the feature of the single-pile mechanism. While, for the inner part, the rigid (H'I'X') and the deforming regions (C'D'E'F'G'A' and A'G'F'I'H') extend to an inclined velocity discontinuity (X'I'F'E') rather than to the x-axis. This discontinuity allows the shift of the flow direction that is necessary to satisfy the velocity boundary condition at the plane of symmetry (y-axis). More details about the mechanism can be found in [Georgiadis et al. \(2013a\)](#).

Subsequently, two new kinematic mechanisms (mechanism A and B) are presented for more practical eccentrically loaded cases. The features of the mechanisms are fully controlled by a set of geometrical parameters, satisfying the boundary conditions of the problem and the plastic flow rule of the material. As the x-axis represents a plane of symmetry with respect to the geometry of the mechanisms and a plane of anti-symmetry with respect to the velocity fields, only half of the mechanisms are considered. This is discussed in the next section.

3.3. Kinematic mechanism A

Mechanism A, shown in [Fig. 7](#), is a variation of the mechanism described in [Georgiadis et al. \(2013a\)](#) for a group of two side-by-side piles. It consists of one rigid

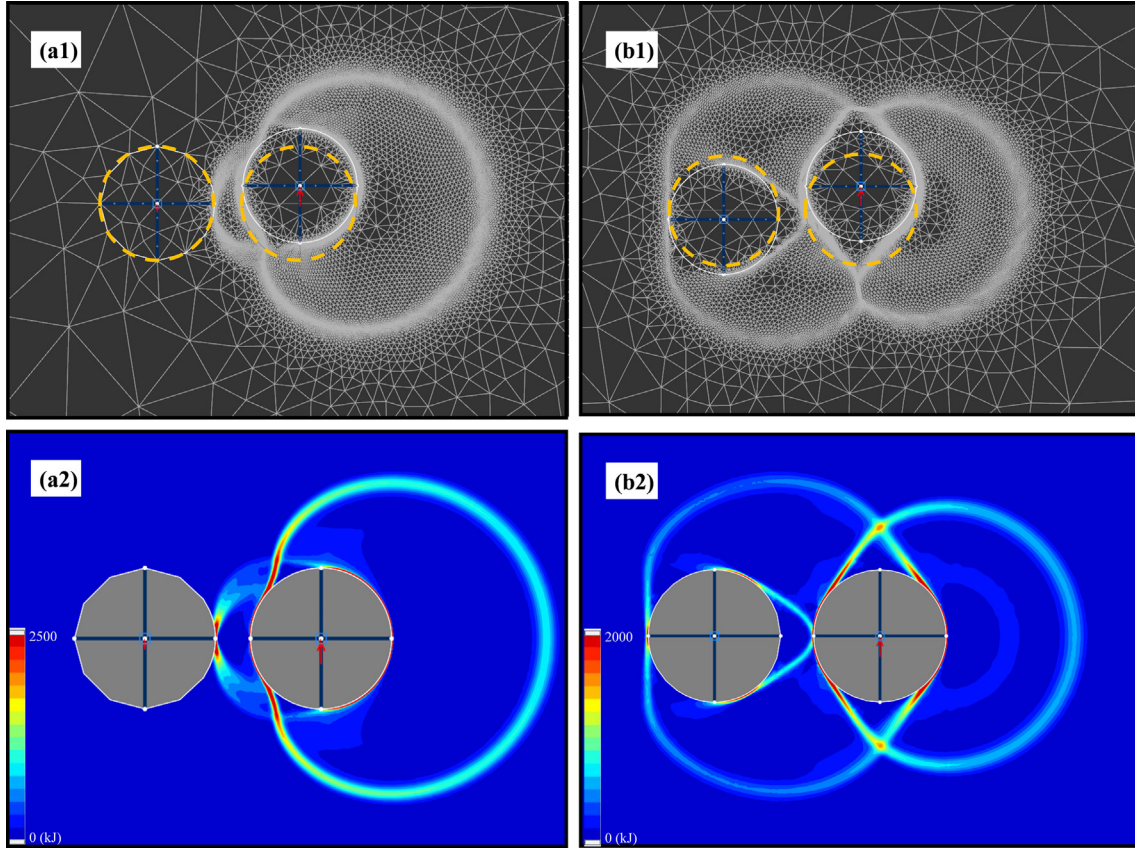


Fig. 4. Failure modes from finite-element limit analysis for $s/D = 1.2$: (a1) finite meshes for $e/s = 0.25$; (a2) power dissipation contour for $e/s = 0.25$; (b1) finite mesh for $e/s = 0.5$; (b2) power dissipation contour for $e/s = 0.5$.

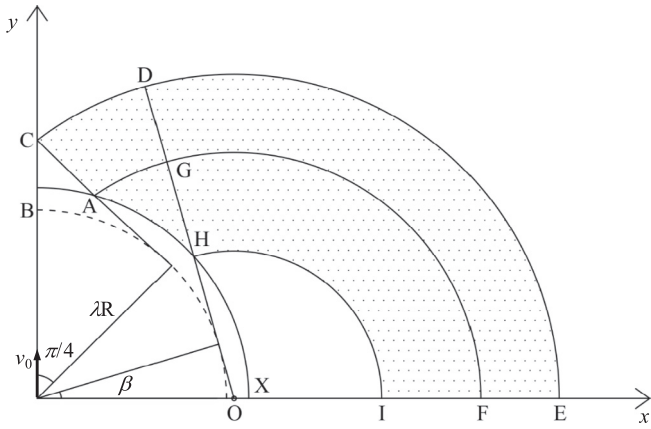


Fig. 5. Kinematic mechanism for single pile (Martin and Randolph, 2006).

region (CX''X'A) translating along the same direction as the RHS pile with velocity v_0 , a rigid body HXI which rotates around point O and several plastically deforming regions (CAGFED, AHIFG and CE'X''). Five optimisation parameters are adopted to describe this mechanism viz. the angles β_1 , β_2 , θ , δ and the normalised radius λ of the evolute of the RHS pile. Note that the RHS part of the mechanism (on the RHS of the plane CT) is essentially based on the Martin-Randolph's mechanism. The only

difference lies on the position of the apex (C) of the rigid body CX''X'A. As it can be seen in Fig. 7, the plane CT presents at an angle ω to the y-axis plane, where the angle ω decreases linearly with increasing pile spacing. This can be expressed as shown in Eq. (4).

$$\omega = \frac{\pi}{4} \frac{s_l/D - s/D}{s_l/D - 1} \text{ for } D \leq s \leq s_l \quad (4)$$

where s_l represents the upper limit pile spacing ratio for the current mechanism obtained from the numerical results.

According to the geometry of the mechanism described in Fig. 7 and Fig. 8, the velocities v and the relative velocities Δv within the regions and discontinuities in the right part of mechanism are presented by the following equations:

Region CAGFED- discontinuities AC and CDE.

$$v = v_0 \sin \beta_1$$

$$\Delta v_{AC} = v_0 \cos \beta_1 \text{ and } \Delta v_{CDE} = v_0 \sin \beta_1 \quad (5)$$

Region AHIFG- discontinuities AH and AGF.

$$v = v_0 \frac{\sin(\rho + \Lambda)}{\lambda}$$

$$\Delta v_{AH} = v_0 \frac{\cos \rho}{\lambda} \text{ and } \Delta v_{AGF} = v_0 \left[\frac{\sin(\beta_1 + \Lambda)}{\lambda} - \sin \beta_1 \right] \quad (6)$$

where $\Lambda = \arccos \lambda$

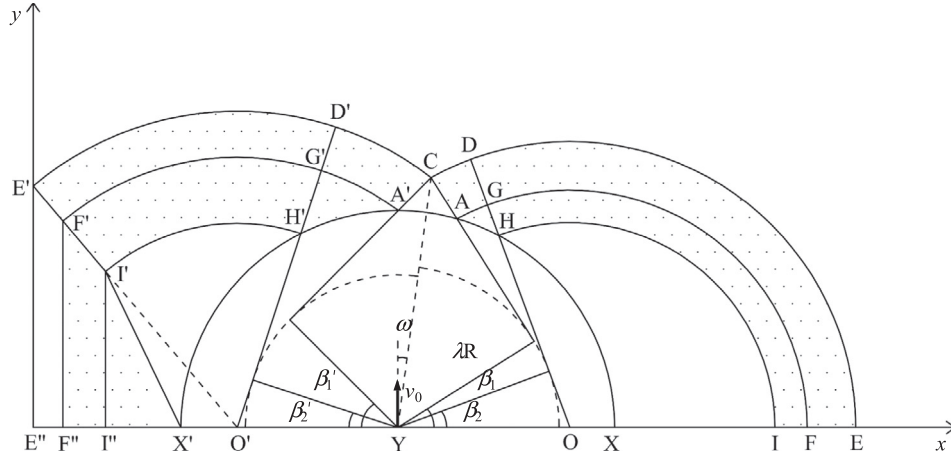


Fig. 6. Kinematic mechanism for two side-by-side piles (Georgiadis et al. 2013a).

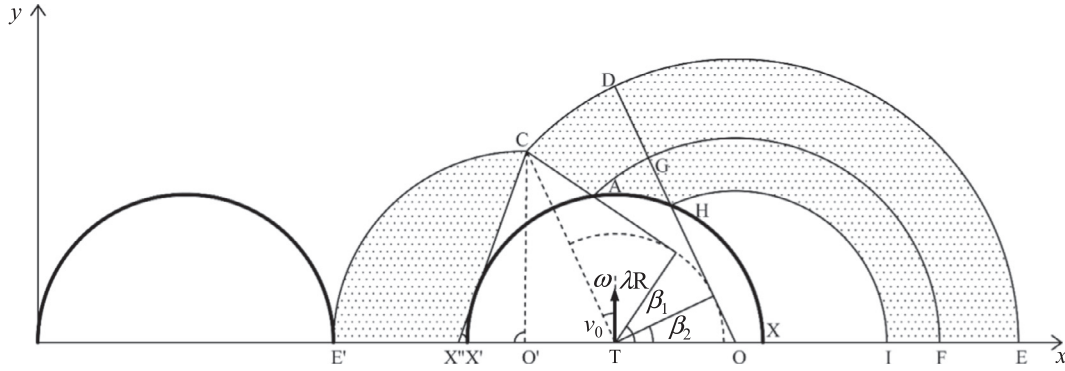


Fig. 7. Kinematic mechanism A. R denotes the pile radius.

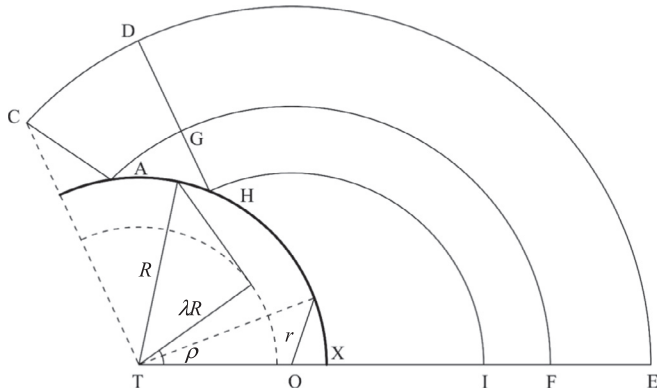


Fig. 8. Geometrical details of the RHS part of mechanism A.

Region HXI- discontinuity HX .

$$v = v_0 \frac{\cos\beta_2}{\lambda R} r \text{ and } \Delta v_{HX} = v_0 \frac{\cos\beta_2}{\lambda} \quad (7)$$

The power dissipation calculations based on the velocity field presented above are similar to those stated in Georgiadis et al. (2013a), and they are not repeated here.

The velocity field pattern in region $CE'X''$, presented in Fig. 9, is derived from the mechanism proposed by Georgiadis et al. (2013b). The velocities associated with

this region are constant along each radius r' and are perpendicular to the line connecting point O' and the point at the outer discontinuity CE' . The magnitude of the velocities v and the velocity jumps Δv within this region and adjacent discontinuities (CX'' and CE') are given as:

$$\begin{aligned} v &= \Delta v_{CE'} \\ &= v_0 \frac{\cos\delta}{\cos(\delta - \theta)} \frac{\sin\delta - \sin(\delta + \theta)\cos\theta}{\sin\delta - \sin(\delta + \theta)\cos\theta'} \text{ and } \Delta v_{CX''} \\ &= v_0 \frac{\sin\theta}{\cos(\delta - \theta)} \end{aligned} \quad (8)$$

Considering the restriction in the geometry of region $CE'X''$, an additional relationship (Eq. (9)) among parameters β_1 , θ and δ is always satisfied during the process of optimisation. The internal power dissipations within this region and associated discontinuities are briefly presented in Appendix.

$$\frac{\lambda R \cos\omega}{\sin(\beta_1 - \omega)} \left[\tan\omega + \cot\delta + \frac{\sin\delta - \sin(\delta + \theta)}{\sin\delta \sin\theta} \right] + R - s = 0 \quad (9)$$

For closely spaced twin-pile group (such as $s/D = 1.2$), mechanism A becomes inapplicable when the eccentricity is greater. Hence, another mechanism corresponding to larger eccentricity case is investigated in the next section.

3.5. Optimisation procedure

As the only external force in this two-dimensional plane-strain problem is the eccentric force imposed on the twin-pile group, the average resistance factor can be calculated through Eq. (16).

$$N_p = \frac{\Delta W_p}{(e/s + 0.5)v_0s_uD} \tag{16}$$

where ΔW_p is the total power dissipated by the stress in half of the twin-pile model.

Following Chen (1992), an optimisation procedure was designed to seek the least upper bound to the undrained resistance factor N_p . See Fig. 11 for the procedure. The

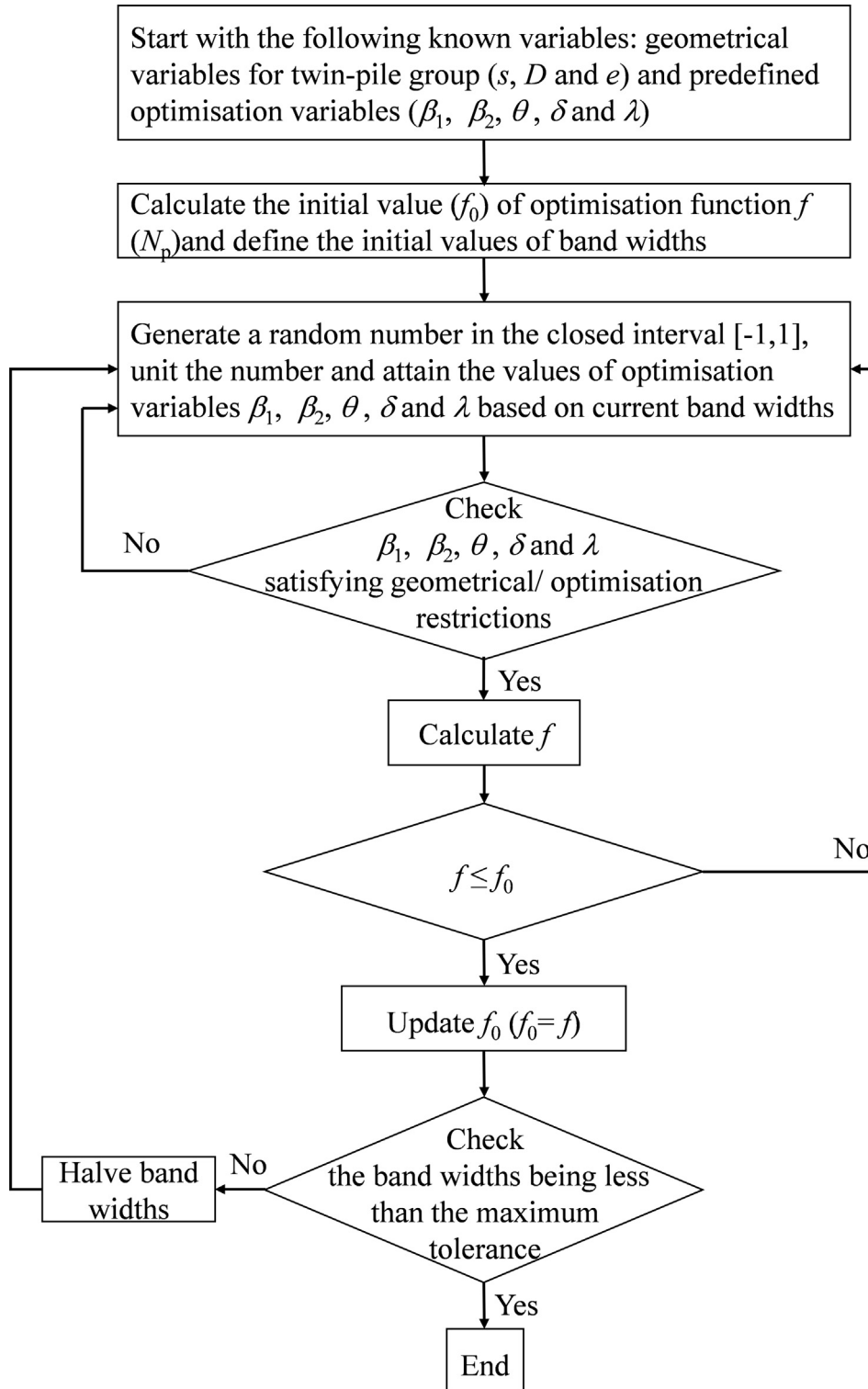


Fig. 11. Optimisation procedure of the upper bound to N_p .

optimisation uses random search to look for the minimum of N_p and performs the minimisation procedure until the band widths of search variables are less than the predefined values. For a twin-pile group of given values of pile spacing s , pile diameter D and loading eccentricity e , variables in the minimisation process include the angles β_1 , β_2 , θ , δ and the normalised radius λ for both mechanism A and mechanism B (see Figs. 5 and 8). In the process of searching for a minimum value of N_p , the relationships among the variables are to be satisfied (Eqs. (9) and (15)), and the optimisation is performed until the band width is less than 0.01 for angles β_1 , β_2 , θ , δ , whilst it is 0.001 for normalised radius λ .

4. Results and discussion

4.1. Comparison of results

Fig. 12 shows a comparison of the resistance factors N_p between the different methods of analysis (i.e. analytical upper bound analysis and numerical upper and lower bound limit analyses). Three normalised pile spacing ratios are presented for $s/D = 1.2$, 1.8 and 2.5. Excellent agreement is observed between the two numerical bounds across the whole range of eccentricities. The difference is extremely small ranging from 0.6% to 2.0%. On the other hand, it can also be seen from Fig. 12 that the analytically calculated solutions are in very good agreement with the numerical results. The difference increases slightly when the eccentricity becomes larger for the special case of a closely spaced pile group ($s/D = 1.2$), but is always within 7%. It should be noted that the gap among the results obtained from different analyses is generally acceptable, even though it can be further narrowed down by optimizing the kinematic velocity field in the analytical calculations, or by using more elements in the numerical simulations. Such a comparison also proves that the mechanisms proposed in this study are capable of predicting the variation of the soil resistance with the eccentricity. The presented upper bound analytical solutions are considered to provide reliable approximations of the ultimate resistance for eccentric loading problems.

4.2. Eccentricity reduction factor G_N

To further quantify the effect of eccentricity on N_p , an eccentricity reduction factor G_N is introduced as follows:

$$G_N = \frac{N_p(\alpha, s, e > 0)}{N_p(\alpha, s, e = 0)} \quad (17)$$

where $N_p(\alpha, s, e > 0)$ denotes the N_p when loading eccentricity exists and $N_p(\alpha, s, e = 0)$ denotes the N_p when loading eccentricity equals zero.

Fig. 13 shows the variations of the eccentricity reduction factor G_N against normalised eccentricity ratio e/s for three

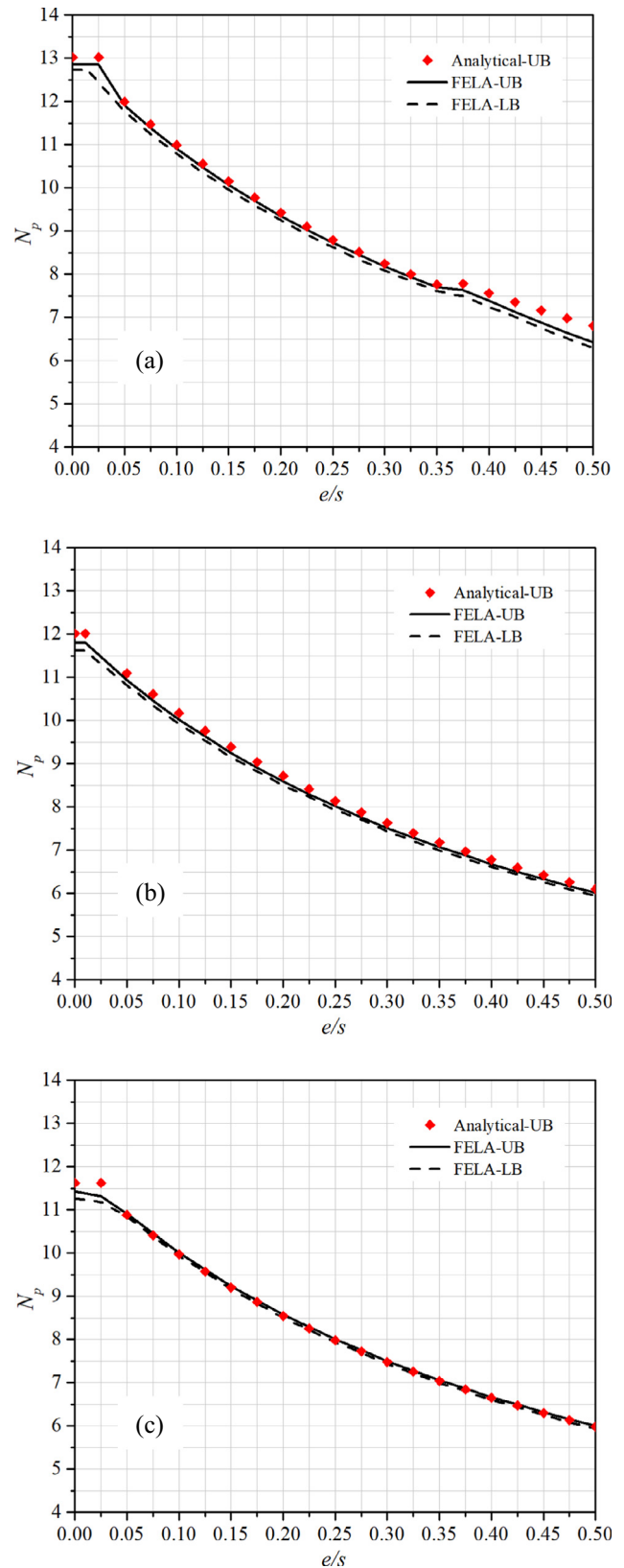


Fig. 12. Comparison of analytically calculated pile resistance factors (Analytical-UB) and upper bound and lower bound finite element limit analyses results (FELA-UB and FELA-LB) for different pile spacing ratios: (a) $s/D = 1.2$, (b) $s/D = 1.8$ and (c) $s/D = 2.5$.

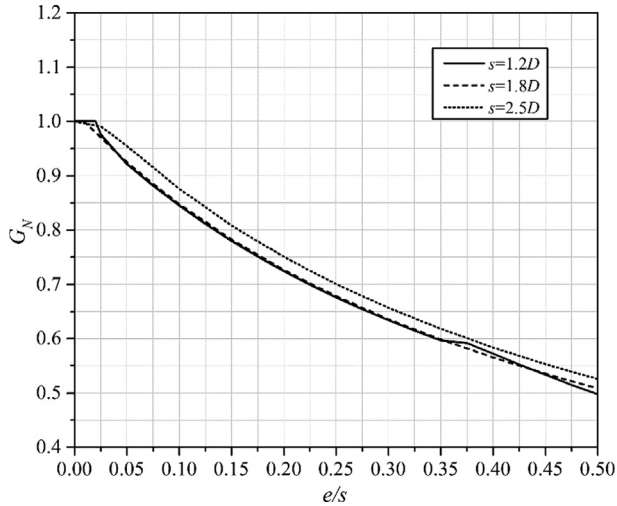


Fig. 13. Variations of the eccentricity reduction factor G_N with e/s for different spacing ratios.

typical pile spacings ratios s/D . As eccentricity increases, G_N generally decreases from unity to around 0.5 for all spacing ratios. Variations of G_N are directly associated with the transformation of failure modes, although they are not much sensitive to the pile spacing. The produced reduction factors in Fig. 13 are useful for practitioners to evaluate the level of reduction in lateral capacity of the twin-pile group due to the presence of loading eccentricity.

4.3. Effect of pile spacing with loading eccentricity

A series of parametric analyses were subsequently conducted to investigate how the pile spacing affects the average pile resistance factor when the loading eccentricity ratio is greater than zero. Shown in Fig. 14 are two sets of results obtained from analytical upper bound analysis

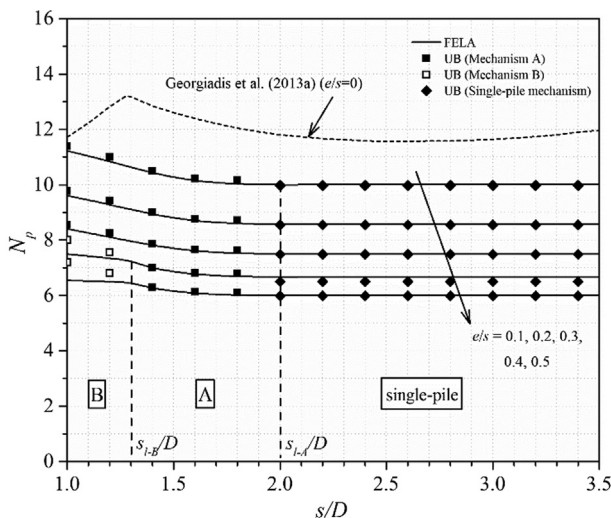


Fig. 14. Variations of the average pile resistance factor N_p with the normalised pile spacing s/D for different eccentricities. Results from Analytical-UB (scattered symbols) and FELA-UB (lines).

and upper bound of FELAs. In analytical upper bound analysis, the ranges of the pile spacing suitable for different mechanisms are determined by observing the failure modes with the aid of FELA analysis. It is worth noting that the presence of eccentricity significantly affects how the spacing influences the ultimate resistance. When $e/s > 0$, N_p generally decreases with the increase in s/D , and it reaches a minimum value for $s/D > 2.0$. This behavior trend is totally different from the case without considering the effect of eccentricity ($e/s = 0$), as reported in Geogiadis et al. (2013a). In addition, the analytical upper bound solutions are in good agreement with the numerical FELA results. The study has concluded that the analytical upper bound solutions can also be confidently used to predict the variation of N_p across the whole range of values of s/D , provided that the postulated mechanism type is correct.

The failure mechanism studies also conclude that the applicable spacing ratios for the failure mechanisms are varied for different values of eccentricity. When e/s is very small such as $e/s = 0.1$ to 0.3 , mechanism A gives the best prediction for the pile spacing $s/D < 2.0$. While for $e/s = 0.4$ and 0.5 , mechanism B is a more suitable choice to predict the N_p for very small spacing ratios ($s/D < 1.3$), and mechanism A is used for the pile spacing between $1.3D$ and $2.0D$. For the pile spacing greater than $2.0D$, the well-defined single-pile mechanism (Martin and Randolph 2006) always gives the optimal estimations in all eccentricity cases investigated.

5. Conclusion

This paper has successfully adopted both finite element limit analysis methods and analytical upper bound plasticity method to investigate the effect of the loading eccentricity and pile spacing on the ultimate lateral resistance of the twin-pile group. Two governing failure mechanisms (mechanisms A and B), associated with different eccentricities and pile spacings, were identified using the rigorous numerical simulations. The two mechanism were then used to establish the framework of analytical upper bound limit analysis. Coupled with the mechanisms introduced by previous researchers, the present kinematic mechanisms form the basis for the derivation of analytical upper bound solutions. These solutions were subsequently compared to the numerical limit analysis results. Excellent agreement is found between the two methods.

Parametric analyses have also suggested that the behavior trend of N_p - s/D curve is totally dissimilar when considering the loading eccentricity. A considerable reduction in the ultimate pile lateral resistance was found as the eccentricity increases. A non-negligible reduction of 50% for rough piles in soft clay was reported. The solutions and mechanisms proposed in this study are particularly valuable for design applications considering loading eccentricity.

It is to be noted that the present two-dimensional plane strain analyses performed in this study focus on the maxi-

imum resistance that may develop along the pile length. The aim of this paper was not to study the distribution of the soil resistance with depth. Thus, the solutions presented are independent of the pile length and they generally correspond to the deeper part of the twin-pile group where the soil is assumed to flow horizontally around the pile shaft. Future work may involve a full 3D analysis with both loading eccentricity and pile length being considered.

Acknowledgements

This study is sponsored by National Natural Science Foundation of China (Grant No. 52008268, Grant No. 51639002 and Grant No. 51809160), Key Laboratory of Ministry of Education for Geomechanics and Embankment Engineering, Hohai University, (Grant No. 20200011). The authors would like to thank OptumCE for providing academic access to OptumG2. The first author also would like to acknowledge the support from The University of Newcastle, Australia, as such study is a continuation of the previous work during the period of his stay in Newcastle, Australia.

Appendix A. Power dissipation calculations in the mechanisms

The dissipation along the velocity discontinuities is,

$$\tau_f \int_L |\Delta v| dL \quad (18)$$

and within the plastically deforming regions is,

$$s_u \int_A |\dot{\epsilon}_{ij}| dA \quad (19)$$

where Δv is the velocity jump along the discontinuity, $\dot{\epsilon}_{ij}$ is the shear strain rate in the region, s_u is the undrained soil shear strength and τ_f represents the ultimate shear stress along the discontinuity (equal to s_u for rough piles, as considered in this study). Some necessary details about mechanism A and B are given in the following, and the rest of the power dissipation calculations can be found in Georgiadis et al. (2013a, 2013b).

A.1. Kinematic mechanism A

The power dissipated within the plastically deforming region CE'X'' and adjacent discontinuities is calculated as the follows:

Discontinuity CX''.

$$D_{CX''} = s_u \Delta v_{CX''} \frac{\lambda R \cos \omega}{\sin(\beta_1 - \omega) \sin \delta} \quad (20)$$

Discontinuities CE'.

$$D_{CE'} = s_u v_0 \frac{\lambda R \cos \omega \cos \delta [\sin \delta - \sin(\delta + \theta) \cos \theta]}{\sin(\beta_1 - \omega) \sin \theta \cos(\delta - \theta)} \times \frac{2 \arctan \left\{ \frac{\tan \frac{\theta}{2} (\sin \delta + \sin(\delta + \theta))}{\sqrt{\sin^2 \delta - \sin^2(\delta + \theta)}} \right\}}{\sqrt{\sin^2 \delta - \sin^2(\delta + \theta)}} \quad (21)$$

Region CE'X''.

The shear strain rate within this region in polar coordinates (ρ', φ') (Fig. 9) is,

$$\dot{\gamma}_{CE'X''} = \frac{v_{CE'X''} \cos(\varphi' - \theta')}{\rho'} - \frac{1}{\rho'} \frac{\partial [v_{CE'X''} \sin(\varphi' - \theta')]}{\partial \varphi'} \quad (22)$$

where $v_{CE'X''}$ is the velocity in region CE'X''.

The internal power dissipation in CE'X'' is calculated as:

$$D_{CE'X''} = s_u \dot{\gamma}_{CE'X''} \rho' d\rho' d\varphi' \quad (23)$$

In addition, the relationship between φ' and θ' is,

$$\varphi' = \arcsin \frac{L_1 \sin \theta'}{\sqrt{L_1^2 + M_1^2 - 2L_1 M_1 \cos \theta'}} = \arcsin N_1 \quad (24)$$

where

$$L_1 = \frac{\lambda R \cos \omega}{\sin(\beta_1 - \omega) \sin \theta} \quad (25)$$

$$M_1 = \frac{\sin(\delta + \theta)}{\sin \delta} \frac{\lambda R \cos \omega}{\sin(\beta_1 - \omega) \sin \theta} \quad (26)$$

Therefore

$$d\varphi' = \frac{1}{\sqrt{1 - N_1^2}} \times \frac{L_1 \cos \theta' (L_1^2 + M_1^2) - L_1^2 M_1 (1 + \cos^2 \theta')}{(L_1^2 + M_1^2 - 2L_1 M_1 \cos \theta')^{\frac{3}{2}}} d\theta' \quad (27)$$

Substituting Eqs. (22) and (27) into Eq. (23) leads to:

$$D_{CE'X''} = s_u v_{CE'X''} \int_0^{\theta} \int_0^{\sqrt{L_1^2 + M_1^2 - 2L_1 M_1 \cos \theta'}} [\cos(\arcsin N_1 - \theta') + \frac{\sin(\delta + \theta) \sin \theta'}{\sin \delta - \sin(\delta + \theta) \cos \theta'} \sin(\arcsin N_1 - \theta')] d\rho' d\theta' \quad (28)$$

A.2. Kinematic mechanism B

The total dissipation for the LHS part of mechanism B includes the power dissipated within one plastically deforming region (CE'O'H'G') and several discontinuities (CH', E'H', H'X', E'T' and CE').

Discontinuity CH'.

$$D_{CH'} = s_u \Delta v_{CH'} L_0 \quad (29)$$

where

$$L_0 = R \left\{ \cot \left[\arcsin \frac{\sin(\beta_1 - \omega)}{\lambda} \right] + \tan \left[\frac{1}{2} \arcsin \frac{\sin(\beta_1 - \omega)}{\lambda} - \frac{\omega}{2} \right] \right\} \quad (30)$$

Discontinuity E'H'

$$D_{E'H'} = s_u \Delta v_{E'H'} L_0 \frac{\sin \delta - \sin(\delta + \theta)}{\sin \theta} \quad (31)$$

Discontinuity H'X'

$$D_{H'X'} = s_u \Delta v_{H'X'} R \tan \left[\frac{1}{2} \arcsin \frac{\sin(\beta_1 - \omega)}{\lambda} - \frac{\omega}{2} \right] \quad (32)$$

Discontinuity E'T'

$$D_{E'T'} = s_u \Delta v_{E'T'} \left\{ L_0 \sin \left[\delta + \arcsin \frac{\sin(\beta_1 - \omega)}{\lambda} - \omega \right] \frac{\sin \delta - \sin(\delta + \theta)}{\sin \theta} + R \tan \left[\frac{1}{2} \arcsin \frac{\sin(\beta_1 - \omega)}{\lambda} - \frac{\omega}{2} \right] \right\} \quad (33)$$

Discontinuity CE'

$$D_{CE'} = s_u v_0 L_0 \sin \delta \frac{[\sin(\delta + \theta) \cos \theta - \sin \delta] \sin \left[\arcsin \frac{\sin(\beta_1 - \omega)}{\lambda} - \omega \right]}{\sin \theta \cos(\delta + \theta)} \times \frac{2 \arctan \left\{ \frac{\tan \frac{\theta}{2} [\sin \delta + \sin(\delta + \theta)]}{\sqrt{\sin^2 \delta - \sin^2(\delta + \theta)}} \right\}}{\sqrt{\sin^2 \delta - \sin^2(\delta + \theta)}} \quad (34)$$

Region CE'O'H'G'

$$D_{CE'O'H'G'} = s_u v_{CE'O'H'G'} \int_0^{\theta} \int_0^{r_0} \left\{ \left[\frac{2}{\sqrt{1-N_2^2}} \frac{L_2 r'^2 \cos \theta' + L_2^2 M_2 \sin^2 \theta'}{r'^3} - 1 \right] \times \cos(\theta' - \arcsin N_2) + \frac{\sin(\delta + \theta) \sin \theta'}{\sin \delta - \sin(\delta + \theta) \cos \theta'} \sin(\theta' - \arcsin N_2) \right\} d\rho' d\theta' \quad (35)$$

where

$$L_2 = \frac{\sin \delta}{\sin \theta} L_0 \quad (36)$$

$$M_2 = -\frac{\sin(\delta + \theta)}{\sin \theta} L_0 \quad (37)$$

$$r_0 = \sqrt{L_2^2 + M_2^2 + 2L_2 M_2 \cos \theta'} \quad (38)$$

$$N_2 = \frac{L_2 \sin \theta'}{r_0} \quad (39)$$

$v_{CE'O'H'G'}$ is the velocity within the region CE'O'H'G', and the definition of ρ' and θ' refers to that in region CE'X'' (Fig. 9).

References

Anderheggen, E., Knöpfel, H., 1972. Finite element limit analysis using linear programming. *Int. J. Solids Struct.* 8 (12), 1413–1431.
 Brown, D.A., Morrison, C., Reese, L.C., 1988. Lateral load behavior of pile group in sand. *J. Geotech. Engrg.* 114 (11), 1261–1276. [https://doi.org/10.1061/\(ASCE\)0733-9410\(1988\)114:11\(1261\)](https://doi.org/10.1061/(ASCE)0733-9410(1988)114:11(1261)).

Brown, D.A., Reese, L., O'Neill, M., 1987. Cyclic lateral loading of a large scale pile group. *J. Geotech. Engrg.* 113 (11), 1326–1343. [https://doi.org/10.1061/\(ASCE\)0733-9410\(1987\)113:11\(1326\)](https://doi.org/10.1061/(ASCE)0733-9410(1987)113:11(1326)).
 Brown, D.A., Shie, C.-F., 1991. Some numerical experiments with a three dimensional finite element model of a laterally loaded pile. *Comput. Geotech.* 12 (2), 149–162.
 Chandrasekaran, S.S., Boominathan, A., Dodagoudar, G.R., 2009. Group interaction effects on laterally loaded piles in clay. *J. Geotech. Geoenviron. Eng.* 136 (4), 573–582. [https://doi.org/10.1061/\(ASCE\)GT.1943-5606.0000245](https://doi.org/10.1061/(ASCE)GT.1943-5606.0000245).
 Chen, Z.-Y., 1992. Random trails used in determining global minimum factors of safety of slopes. *Can. Geotech. J.* 29 (2), 225–233.
 Christensen, H., Niewald, G., 1992. Laterally loaded piles in clay. In: *Proc. 11th Nordic Geotechnical Meeting NGM-92*, Aalborg, 2, pp. 405–10.
 Cox, W.R., Reese, L.C., Crubbs, B.S., 1984. Lateral load tests of 25.4 mm diameter piles in very soft clay in side-by-side and in-line groups. In: *Langer, J.A., Mosley, E.T., Thompson, C.D. (Eds.) Laterally loaded deep foundations: Analysis and performance ASTM SPT 835*. ASTM, West Conshohocken, PA.
 Georgiadis, K., Sloan, S.W., Lyamin, A.V., 2013a. Ultimate lateral pressure of two side-by-side piles in clay. *Géotechnique* 63 (9), 733–745.
 Georgiadis, K., Sloan, S.W., Lyamin, A.V., 2013b. Effect of loading direction on the ultimate lateral soil pressure of two piles in clay. *Géotechnique* 63 (13), 1170–1175.
 Georgiadis, K., Sloan, S.W., Lyamin, A.V., 2013c. Undrained limiting lateral soil pressure on a row of piles. *Comput. Geotech.* 54 (Oct), 175–184.
 Georgiadis, K., Sheil, B., 2020. Effect of torsion on the undrained limiting lateral resistance of piles in clay. *Géotechnique* 70 (8), 700–710.
 Hazzar, L., Hussien, M.N., Karray, M., 2017. Vertical load effects on the lateral response of piles in layered media. *Int. J. Geomech.* 17 (9), 04017078. [https://doi.org/10.1061/\(ASCE\)GM.1943-5622.0000970](https://doi.org/10.1061/(ASCE)GM.1943-5622.0000970).
 Ilyas, T., Leung, C.F., Chow, Y.K., Budi, S.S., 2004. Centrifuge model study of laterally loaded pile groups in clay. *J. Geotech. Geoenviron. Eng.* 130 (3), 274–283. [https://doi.org/10.1061/\(ASCE\)1090-0241\(2004\)130:3\(274\)](https://doi.org/10.1061/(ASCE)1090-0241(2004)130:3(274)).
 Klar, A., Osman, A.S., 2008. Continuous velocity fields for the T-bar problem. *Int. J. Numer. Anal. Meth. Geomech.* 32 (8), 949–963.
 Krabbenhoft, K., Lyamin, A.V., Hjiaj, M., Sloan, S.W., 2005. A new discontinuous upper bound limit analysis formulation. *Int. J. Numer. Methods Engrg* 63 (7), 1069–1088.
 Krabbenhoft, K., Lyamin, A., Krabbenhoft, J., 2017. *OptumG2: Theory manual*. Optum Computational Engineering. Accessed May 25, 2017. <https://www.optumce.com/wp-content/uploads/2016/05/Theory.pdf>.
 Krabbenhoft, K., Lyamin, A.V., Sloan, S.W., 2007. Formulation and solution of some plasticity problems as conic programs. *Int. J. Solids Struct.* 44 (5), 1533–1549.
 Lyamin, A.V., Sloan, S.W., 2002a. Lower bound limit analysis using nonlinear programming. *Int. J. Numer. Methods Engrg* 55 (5), 573–611.
 Lyamin, A.V., Sloan, S.W., 2002b. Upper bound limit analysis using linear finite elements and nonlinear programming. *Int. J. Numer. Anal. Methods Geomech.* 26 (2), 181–216.
 Lysmer, J., 1970. Limit analysis of plane problems in soil mechanics. *J. Soil Mech. Found. Div. ASCE* 96 (4), 1311–1334.
 Martin, C.M., Randolph, M.F., 2006. Upper-bound analysis of lateral pile capacity in cohesive soil. *Géotechnique* 56 (2), 141–145.
 Matlock, H., 1970. Correlations for design of laterally loaded piles in soft clay. In: *Proc. Offshore Technol. Conf. Houston, TX, OTC 1204*.
 Matlock, H., Ingmar, W.B., Kelley, A.E., Bogard, D., 1980. Field tests of lateral load behavior of pile groups in soft clay. *Proc., 12th Annual Offshore Technology Conf. OTC 3871*.
 McVay, M., Bloomquist, D., Vanderlaine, D., Clausen, J., 1994. Centrifuge modeling of laterally loaded pile group in sand. *Geotech. Test. J.* 17 (2), 29–137.

- Chaney, R.C., Demars, K., McVay, M.C., Shang, T.-I., Casper, R., 1996. Centrifuge testing of fixed-head laterally loaded battered and plumb pile groups in sand. *Geotech. Test. J.* 19 (1), 41. <https://doi.org/10.1520/GTJ11406J>.
- McVay, M., Zhang, L., Molnit, T., Lai, P., 1998. Centrifuge testing of large laterally loaded pile groups in sands. *J. Geotech. Geoenviron. Eng.* 124 (10), 1019–1026. [https://doi.org/10.1061/\(ASCE\)1090-0241\(1998\)124:10\(1016\)](https://doi.org/10.1061/(ASCE)1090-0241(1998)124:10(1016)).
- Murff, J.D., Hamilton, J.M., 1993. P-ultimate for undrained analysis of laterally loaded piles. *J. Geotech. Engrg.* 119 (1), 91–107. [https://doi.org/10.1061/\(ASCE\)0733-9410\(1993\)119:1\(91\)](https://doi.org/10.1061/(ASCE)0733-9410(1993)119:1(91)).
- Murff, J.D., Wagner, D.A., Randolph, M.F., 1989. Pipe penetration in cohesive soil. *Géotechnique* 39 (2), 213–229.
- Pan, J.L., Goh, A.T.C., Wong, K.S., Teh, C.I., 2000. Model tests on single piles in soft clay. *Can. Geotech. J.* 37 (4), 890–897.
- Pham, Q.N., Ohtsuka, S., Isobe, K., Fukumoto, Y., 2019. Group effect on ultimate lateral resistance of piles against uniform ground movement. *Soils Found.* 59 (1), 27–40.
- Poulos, H.G., 1971. Behavior of laterally loaded piles I. single piles. *J. Soil Mech. Found. Div.* 97 (5), 711–731.
- Randolph, M.F., Houlsby, G.T., 1984. The limiting pressure on a circular pile loaded laterally in cohesive soil. *Géotechnique* 34 (4), 613–623.
- Reese, L.C., Welch, R.C., 1975. Lateral loading of deep foundations in stiff clay. *J. Geotech. Engrg Div. ASCE* 101 (7), 633–649.
- Rollins, K.M., Olsen, K.G., Jensen, D.H., Garrett, B.H., Olsen, R.J., Egbert, J.J., 2006. Pile spacing effects on lateral pile group behavior: Analysis. *J. Geotech. Geoenviron. Eng.* 132 (10), 1272–1283. [https://doi.org/10.1061/\(ASCE\)1090-0241\(2006\)132:10\(1272\)](https://doi.org/10.1061/(ASCE)1090-0241(2006)132:10(1272)).
- Sheil, B.B., 2021. Lateral limiting pressure on square pile groups in undrained soil. *Géotechnique* 71 (4), 279–287. <https://doi.org/10.1680/jgeot.18.P.118>.
- Shiau, J., Smith, C., 2006. Numerical analysis of passive earth pressures with interfaces. In: *Proc., 3rd European Conf. on Computational Mechanics*, 147. Springer, Dordrecht, The Netherlands.
- Shiau, J.S., Augarde, C.E., Lyamin, A.V., Sloan, S.W., 2008. Finite element limit analysis of passive earth resistance in cohesionless soils. *Soils Found.* 48 (6), 843–850. <https://doi.org/10.3208/sandf.48.843>.
- Shiau, J., 2016. Introducing advanced topics in geotechnical engineering teaching – tunnel modelling. *Int. J. Geomate*. <https://doi.org/10.21660/2016.19.150625>.
- Shiau, J., Al-Asadi, F., 2020. Three-dimensional analysis of circular tunnel headings using Broms and Bennermarks' original stability number. *Int. J. Geomech.* 20 (7), 06020015. [https://doi.org/10.1061/\(ASCE\)GM.1943-5622.0001734](https://doi.org/10.1061/(ASCE)GM.1943-5622.0001734).
- Sloan, S.W., 1988. Lower bound limit analysis using finite elements and linear programming. *Int. J. Numer. Anal. Methods Geomech.* 12 (1), 61–77.
- Sloan, S.W., 1989. Upper bound limit analysis using finite elements and linear programming. *Int. J. Numer. Anal. Methods Geomech.* 13 (3), 263–282.
- Sloan, S.W., 2013. Geotechnical stability analysis. *Geotechnique*. 63 (7), 531–571.
- Su, D., Zhou, Y.G., 2016. Effect of loading direction on the response of laterally loaded pile groups in sand. *Int. J. Geomech.* 16 (2), 04015051. [https://doi.org/10.1061/\(ASCE\)GM.1943-5622.0000544](https://doi.org/10.1061/(ASCE)GM.1943-5622.0000544).
- Teramoto, S., Niimura, T., Akutsu, T., Kimura, M., 2018. Evaluation of ultimate behavior of actual large-scale pile group foundation by in-situ lateral loading tests and numerical analysis. *Soils Found.* 58 (4), 819–837.
- Ueda, K., Sawada, K., Wada, T., Tobita, T., Iai, S., 2019. Applicability of the generalized scaling law to a pile-inclined ground system subject to liquefaction-induced lateral spreading. *Soils Found.* 59 (5), 1260–1279.
- Yu, J., Huang, M., Leung, C.F., Li, S., 2017. Upper bound solution of a laterally loaded rigid monopile in normally consolidated clay. *Comput. Geotech.* 91 (Nov), 131–145.
- Yu, J., Huang, M., Zhang, C., 2015. Three-dimensional upper-bound analysis for ultimate bearing capacity of laterally loaded rigid pile in undrained clay. *Can. Geotech. J.* 52 (11), 1775–1790.
- Zhang, L., Zhao, M., Zou, X., 2013. Behavior of laterally loaded piles in multilayered soils. *Int. J. Geomech.* 15 (2), 06014017. [https://doi.org/10.1061/\(ASCE\)GM.1943-5622.0000319](https://doi.org/10.1061/(ASCE)GM.1943-5622.0000319).
- Zhao, T., Wang, Y., 2018. Interpretation of pile lateral response from deflection measurement data: A compressive sampling-based method. *Soils Found.* 58 (4), 957–971.
- Zhao, Z., Kouretzis, G., Sloan, S.W., Gao, Y., 2017a. Ultimate lateral resistance of tripod pile foundation in clay. *Comput. Geotech.* 92 (Dec), 220–228.
- Zhao, Z., Li, D., Zhang, F., Qiu, Y., 2017b. Ultimate lateral bearing capacity of tetrapod jacket foundation in clay. *Comput. Geotech.* 84 (Apr), 164–173.
- Zhao, Z., Kouretzis, G., Sloan, S.W., Gao, Y., 2019. Effect of geometric nonlinearity on the ultimate lateral resistance of piles in clay. *Comput. Geotech.* 105 (Jan), 110–115.
- Zhao, Z., Gao, Y., 2019. Effect of loading eccentricity on the ultimate lateral resistance of tripod piles in clay. *Geotech. Lett.* 9 (2), 106–115.